

Wafer-Level Self-Organized Copolymer Templates for Nanolithography with Sub-50 nm Feature and Spatial Resolutions

Sivashankar Krishnamoorthy,* Krishna Kumar Manipaddy, and Fung Ling Yap

Robust lithographic templates, with sub-50 nm feature and spatial resolutions, that exhibit high patterning integrity across a full-wafer are demonstrated using self-organized copolymer reverse micelles on 100 mm Si wafers. A variation of less than 5% in the feature size and periodicity of polymeric templates across the entire wafer is achieved simply by controlling the spin-coating process. Lithographic pattern transfer using these templates yields Si nanopillar arrays spanning the entire wafer surface and exhibiting high uniformity inherited from the original templates. The variation in geometric characteristics of the pillar arrays across the full-wafer surface is validated to be less than 5% using reflectance spectroscopy. The physical basis of the change in reflectance with respect to sub-10 nm variations in geometric parameters of pillar arrays is shown by theoretical modelling and simulations. Successful fabrication of highly durable TiO₂ masks for nanolithography with sub-50 nm feature width and spatial resolutions is achieved through highly controlled vapour phase processing of reverse micelle templates. This allows lithographic pattern-transfer of organic templates with a feature thickness and separation of less than 10 nm, which is otherwise not possible through other approaches reported in literature.

1. Introduction

The need for higher performance and miniaturization of devices has raised considerable demand for small scale structures, pushing feature size and spatial resolutions down to sub-50 nm length scales. Such patterns are of high interest for applications in photovoltaics,^[1] plasmonics,^[2] solid-state lighting,^[3] sensors,^[4] energy storage,^[5] molecular separation,^[6] and patterned media.^[7] Lithography is a promising means of creating such structures with well-defined feature size, periodicity, and with different combinations of technologically relevant materials and substrates. Nanoscale templates for lithography down to sub-50 nm pattern resolutions can be produced using state of the art techniques^[8–10] such as e-beam lithography, nanostencils,^[11,12] X-ray interference, and double exposure patterning

with deep UV radiation. However, these techniques encounter the challenges of a) high fabrication costs, b) low throughput, and c) templates lacking durability when the size and periodicity is scaled down. Alternative approaches that allow parallel fabrication of robust, high-resolution lithographic templates over full wafer level are essential for building viable technologies for adoption by industry. Pattern integrity across wafer level is crucial to ensure that the devices fabricated across different parts of the wafer exhibit the same characteristics. Microphase separation of block copolymers^[13–15] in thin films has been widely investigated for nanolithography applications,^[16,17] and the ability to vary size, periodicity, and morphology have been convincingly demonstrated.^[18,19] However, the process is multi-step and involves time-consuming steps such as surface neutralization and annealing of polymer films, each of which can cost several hours. Furthermore, when a large number of steps is

involved, each processing step can introduce a certain level of non-uniformity. This also makes it difficult to ensure pattern integrity across whole areas of full wafers.^[20] A much simplified and direct approach, especially for achieving 2D dot array patterns, is the use of spherical reverse micelles of amphiphilic copolymers.^[21,22] Spherical reverse micelles are soft polymeric nanoparticles that can be deposited on a surface and used as such for lithography. The possibility of using reverse micelles in nanolithography has been presented in earlier reports.^[23–25] These papers, however, do not address key limitations that prevent the use of this approach for nanolithography when the features on the template have a thickness or separation approaching sub-10 nm scale. The latter situation is invariably encountered, however, when ultrahigh feature and spatial resolutions are sought. Furthermore, the earlier work does not address the unique challenges of achieving uniform patterns of reverse micelles, particularly when coated over large areas such as full wafers. Since annealing above the glass transition temperature of the copolymer destroys reverse micelle-based patterns, the uniformity must be achieved as-coated without additional processing. In this report, we overcome these challenges and convincingly demonstrate

Dr. S. Krishnamoorthy, Dr. K. K. Manipaddy, Dr. F. L. Yap
Institute of Materials Research and Engineering (IMRE)
Agency for Science Technology and Research (A*STAR)
3 Research Link, 117602, Singapore
E-mail: krishnamoorthys@imre.a-star.edu.sg

DOI: 10.1002/adfm.201002380

nanolithography using high-resolution reverse micelle patterns over 100-mm silicon wafers.

2. Full-Wafer Templates for Nanolithography

2.1. Template Characteristics

In order to achieve uniform templates over a full wafer, it is essential to have a clear understanding of the pattern formation as well as the origin of non-uniformities in feature width, periodicity, and topography of the templates. This is best carried out through a detailed analysis of the structure of reverse micelles in solution and its relation to the nanopatterns formed on the surface. Earlier literature on reverse micelle-based patterning offers limited understanding on this aspect. However, this understanding is important in order to determine or predict the lithographic outcome for the geometric attributes of the nanostructures resulting from these templates. Reverse micelles of polystyrene-block-poly(2-vinylpyridine) PS-*b*-P2VP were obtained by dissolving the copolymer in *m*-xylene. Core-shell particles with PS shell and P2VP core were formed due to selective dissolution of the PS block by xylene.^[26] Thin films of reverse micelles were created by spin-coating the solution at 5000 rpm on 1 cm × 1 cm chips, and used for preliminary

studies. PS-*b*-P2VP with a molecular weight of 80.5 kDa, a volume fraction of PS block (f_{PS}) of ~0.5, and PDI (M_w/M_n) of 1.1, was used for these experiments. **Figure 1a** shows statistics for size distributions of reverse micelles in solution, as obtained from dynamic light scattering (DLS) measurements. DLS measurements reveal a mean diameter of 68 nm and a standard deviation of 5.5% (expressed as coefficient of variance in percentage, i.e., $\sigma/\text{mean} \times 100$) (D_h , Figure 1a). This represents the size of the reverse micelles in a swollen state in the solution phase before their deposition on the surface. A continuous film consisting of hemispherical features exhibiting a 2D quasi-hexagonally ordered arrangement (Figure 1b top, Figure 2a) was obtained when coated from micelle solutions with concentrations in the range of 0.6–1.0% (w/w). At lower concentrations, the monolayer exhibits patchy coverage and at high concentrations, multilayers are formed. Figure 1b shows distribution in geometric variables (height, diameter, and periodicity) of the patterns, obtained from the statistical analysis of pixels in atomic force microscopy (AFM) images. Mean height and diameter of the polymeric features were thus determined to be 28 nm and 56 nm respectively. The periodicity was determined to be 68, 74, and 79 nm for coatings prepared from solutions with concentrations of 1.0%, 0.8% and 0.6% (Figure 1b, d_1 , d_2 , d_3) respectively. The distribution in array periodicity was determined from a 2D power spectral density (PSD) function,

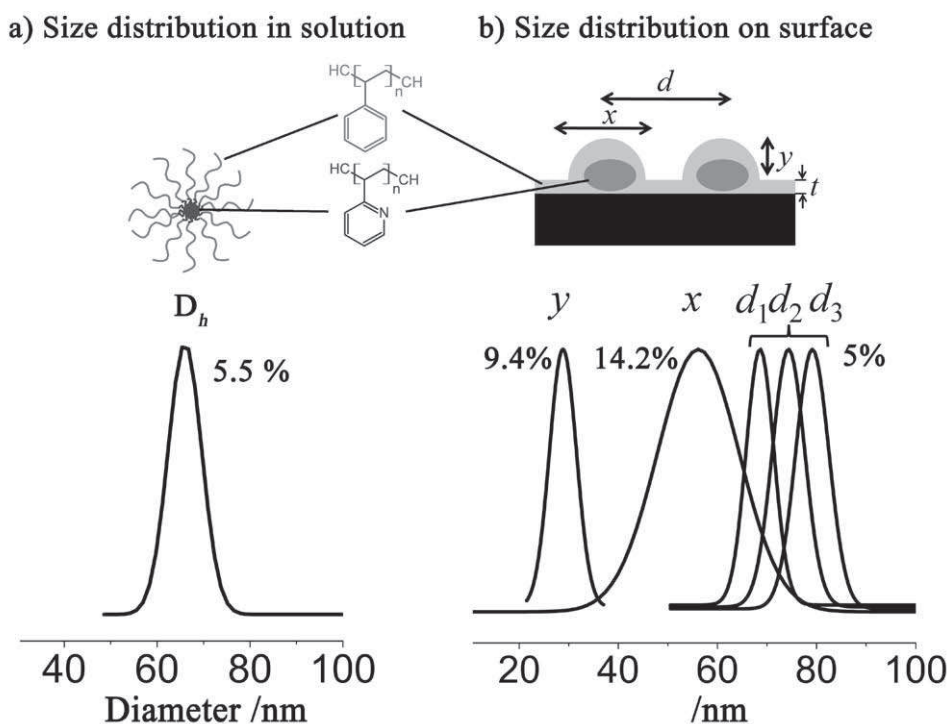


Figure 1. Schematic comparing size distributions of PS-*b*-P2VP (M_w of 80.5 kDa, $f_{PS} \sim 0.5$). a) spherical reverse micelles in solution-phase with b) nanoscale patterns obtained on surface. The percentages indicated against the curves represent the coefficient of variation in percent for the respective distributions. a) (top) schematic of the micelle structure in solution and (bottom) the distribution in hydrodynamic size (D_h) in *m*-xylene solution, as measured using DLS. b) (top) schematic showing a cross-section of a thin film of reverse micelles on surface. (bottom) Normalized Gaussian distributions of height (y), diameter (x) and periodicity (d) of micelle arrays obtained. All curves were obtained from image analysis of tapping mode AFM measurements of the micelle films coated from *m*-xylene solutions. The curves for y and x correspond to films coated from solutions with concentrations of 0.6% (w/w), while curves for d_1 , d_2 , d_3 correspond to concentrations of 1.0%, 0.8%, 0.6% (w/w), respectively.

which relates the amplitude of topography as a function of the spatial frequency of topography. The trend of increasing periodicity with decreasing concentration is in accordance with earlier reports.^[27]

In comparing the DLS and AFM data above, it can be seen that the array periodicity of the patterns on the surface is primarily determined by the diameter of reverse micelles in the solvated form when in solution. This can be inferred from the fact that the minimum value of 68 nm observed in the periodicity of the surface patterns was found to agree well with the hydrodynamic size of the reverse micelles in solution phase. The maximum periodicity attainable was found to be ~20% higher than the mean diameter of the micelles in solution. Such a possibility for tunability in array periodicity can be explained only by taking into account the contribution due to deformation of the solvated reverse micelles when being spaced on the surface during pattern-formation. Such deformation can allow an increase in array periodicity only until such a point where the swollen PS block from the reverse micelles in its deformed state can reach out to fuse with PS block from adjacent micelle. If this condition is not met, a patchy coverage ensues. Such patchy coverage is therefore typically encountered at low solution concentration or high spin-speeds when the reverse micelles are spaced significantly far apart.

In addition to the peak values for the distributions in size and periodicity, comparison of the peak widths also provides valuable information on nanopattern formation. It can be observed from Figure 1 that the standard deviation in the array periodicity of ~5% agrees well with that of size distribution of micelles in solution for all three curves (d_1 , d_2 , d_3) shown. This agreement is to be expected when the array periodicity is determined by the diameter of the reverse micelles in their solvated form. However, it can be observed that the standard deviation in template topography as well as feature width is more than double that of the reverse micelles in solution (Figure 1a, 1b). This broadening in size distribution from solution phase to surface can be explained as resulting from the statistical variation in the extent of deformation between individual micelles across the array. The observed standard deviation in feature sizes agrees well with the typical magnitudes of size distribution expected of self-assembled systems such as colloidal particles^[28] or copolymers^[29] reported in literature.

In addition, besides the distribution in height, diameter, and periodicity, the quality of lateral order is an additional aspect of significant interest in evaluating the nanopatterns. Although the PSD analysis is a reliable means of assessing the standard deviation in periodicity, the quality of spatial order in the 2D array is best assessed through the radial distribution function ($g(r)$), also known as pair correlation function). The $g(r)$ plot for an as-coated array of reverse micelles is shown in Figure 2b. The absolute radial distance in the x -axis is normalized with the value of array periodicity obtained from 2D PSD analysis. The peak positions of the $g(r)$ oscillations agree well with integral multiples of the array periodicity, as expected for a hcp lattice. The $g(r)$ oscillations are found to propagate to a distance equivalent to 10 times the array periodicity, or an absolute radial distance of ~800 nm. This indicates an average size of ~1.6 μm for the ordered domains. For phase-separated copolymer thin films, a similar quality of ordering is shown to be attained after

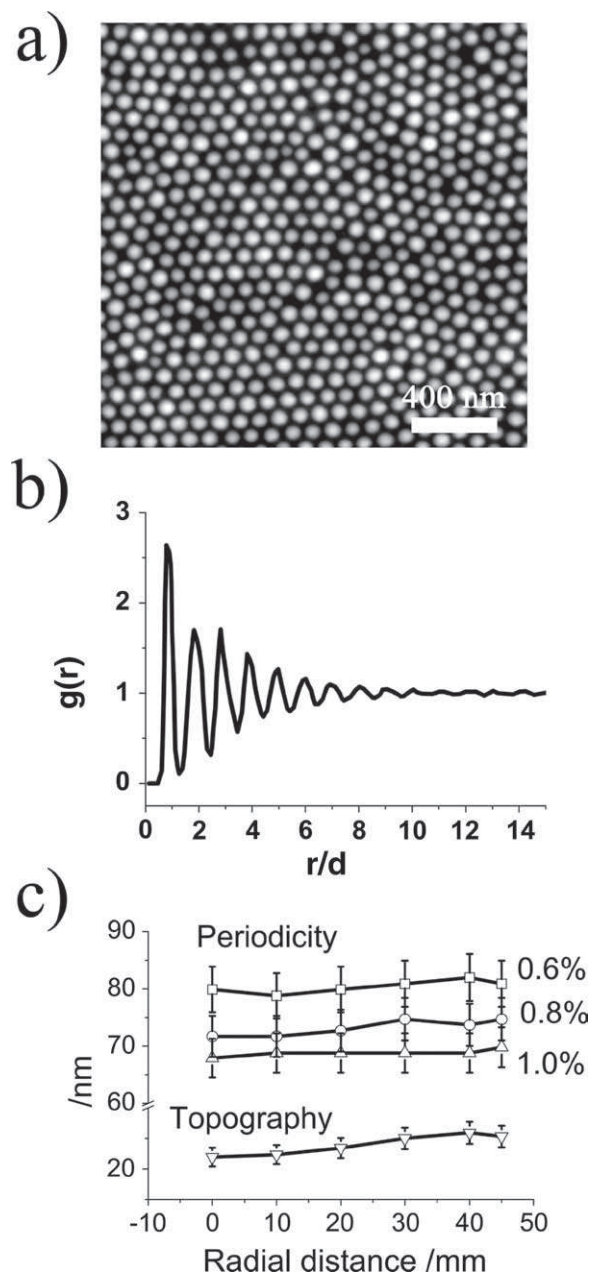


Figure 2. a) Tapping mode AFM image of a representative monolayer of the PS-b-P2VP (M_w of 80.5 kDa, $f_{PS} \sim 0.5$, coated from 0.6% solution of *m*-xylene) reverse micelle arrays on silicon substrate. Grain boundary defects between ordered domains can be seen. b) Plot showing radial distribution function $g(r)$ as a function of normalized radial distance (r), obtained by analyzing AFM image of micelle arrays measured over an area of $5 \mu\text{m} \times 5 \mu\text{m}$. The radial distance was normalized using the average array periodicity (d) as the normalization constant, which was taken to be 78.8 nm. The excellent agreement between the observed peak positions with integral multiples of r/d can be seen. c) Plot of topography or periodicity as a function of radial distance from the centre (0 mm) to the edge (50 mm) of the wafer with the last point measured at 45 mm.

several steps of optimization requiring much longer durations of time.^[30] In the case of micelle patterns, the ability to produce such ordered patterns even in the as-coated form is one of its chief advantages. Further post-processing can be performed

using solvent annealing to induce long-range ordering of the copolymer domains. However, such post-processing is also known to result in macroscopic dewetting which would necessitate considerable attention to ensure integrity of the ordered films across large areas.^[31]

2.2. Full-Wafer Templates

When depositing the reverse micelles on a complete wafer, maintaining the integrity of the resulting patterns on different areas of the wafer is of high importance. As discussed earlier, the periodicity of the reverse micelle arrays is sensitive to the coating conditions and can result in a variation as high as 20%. Such a value of variation refers only to cases where a continuous array of reverse micelles is obtained, without patchy coverage or multilayer formation. During spin-coating of polymer films on large areas such as a wafer, a radial thickness variation (or decrease) can be expected from the centre to edge of the wafer. The thickness variations can result from non-Newtonian flow behavior of the polymer solutions during spin-coating.^[32] The study on non-Newtonian flow behavior of diblock copolymer micelles by Watanabe et al. is of interest in this context.^[33] Earlier work on theoretical and experimental investigations^[32,34,35] on spin-coating have shown that the radial uniformity of the spin-coated polymer films can be significantly influenced by both the duration required to attain the set spin-speed (or acceleration) and the spin speeds used. Flack et al.^[34] showed that a low acceleration setting contributed to an increase in the radial thickness gradient across the wafer, and thus greater non-uniformity. Although their study pertains to continuous homopolymer films, we found this to be true in case of reverse micelle coatings as well. In the case of reverse micelle coatings, such thickness variations manifest as a difference in pitch or array periodicity of the reverse micelle array. It was observed that the coatings exhibited the lowest variation in periodicity when coated at high acceleration and spin-speed. For the 80.5 kDa system shown in Figure 1, coating at spin-coating speed of 5000 rpm and acceleration of 5000 rpm/s using solution concentrations of 0.6–1.0% (w/w), produced reverse micelle arrays with variation of <5% in periodicity across the complete wafer. The radial uniformity in template characteristics were measured by recording AFM images every 10 mm from the centre to edge of the wafer. A representative AFM image recorded in tapping mode is shown in Figure 2a. The variation in topography and the periodicity across wafer was measured by comparing the peak as well as the width of the distribution of their respective histograms. The plot in Figure 2c shows variation in periodicity and topography for a highly uniform array coated on a 100 mm silicon wafer. Three different curves shown for the periodicities correspond to the different concentrations (0.6%, 0.8%, and 1.0%) that were used for coating. The trend of decreasing values of periodicity with increasing solution concentration is clearly discernable. The topography shown in Figure 2c corresponds to coatings made from 0.6% solution concentration and was found to be uniform across the entire film. The uniformity in topography was confirmed in a similar way for all wafer-level coatings, made at other concentrations. Despite the high accuracy of AFM in measuring surface

topography, care needs to be exercised while determining the height of features that are separated by tiny distances. Separations below 10 nm can be subject to tip-convolution effects due to the inability of the tip to reach the surface, therefore resulting in under-reporting of height values.

The well-controlled, consistent, and high-precision templates demonstrated here are well-suited to use as lithographic templates for the creation of highly uniform etched structures on desired substrates by dry etching. Pattern transfer by dry etching is a well-established technique, allowing etching into a variety of substrates such as Si, SiO₂, Si₃N₄, and III–V semiconductors. Amongst the most limiting factors in performing high-resolution nanolithography is the robustness and uniformity of the template itself. Ensuring the latter allows realizing etched structures that are free from challenges of overlapping domains, missing features, or broad feature distributions for width, height, and periodicity. In the following, silicon pillar arrays exhibiting such uniformity and integrity spanning full wafers are demonstrated.

3. Pattern-Transfer to Create Si Pillar Arrays Over Full-Wafer and Validating Uniformity

We demonstrate the effective translation of the uniformity of organic templates shown in Section 2, into silicon nanopillar arrays obtained via lithographic pattern transfer. Silicon nanopillar arrays with high density as well as uniformity are sought after in different applications such as biosensors,^[36] capacitors,^[37,38] batteries,^[5,39] solar cells,^[40,41] and photonic crystal wave guides.^[42] It should be noted that the lack of long-range order in the patterns obtained does not affect their utilization for many of these applications. A perfect ordering is necessary only when addressability of individual nanostructures is sought, e.g., in bit-patterned media, or when periodicity introduces special properties, e.g., photonic crystals. Most other applications rely on averaged properties of nanoassemblies such as high feature densities, high interfacial surface areas, and effective refractive index. However, even in the latter cases, it is essential to achieve nanopatterns with high reproducibility, narrow standard deviations, and high spatial uniformity via convenient and flexible fabrication routes. These are advantages that are typical of the patterning approaches presented throughout this report.

Lithographic pattern transfer of the polymer templates onto an underlying Si substrate was performed through a two-step process as described in literature (Figure 3a).^[24,43] The reverse micelles obtained from the 80.5 kDa system were coated on Si wafer having a 25 nm film of thermally grown SiO₂ layer. The micelle templates were first treated with brief O₂ plasma to isolate the bumps and expose the substrate beneath. This process helps in removal of the continuous layer of PS layer with thickness (*t*, Figure 1b top) of ~2–3 nm that is formed due to the fusion of coronal PS blocks between adjacent micelles during their deposition on substrate. The resulting polymer templates are then transferred into underlying SiO₂ film using C₄F₈/CH₄ plasma. The SiO₂ particle masks formed provide a much higher selectivity than do polymeric templates in the subsequent reactive ion etching (RIE) step in which Si is etched by a Cl₂ based plasma. The uniformity of the resulting Si pillar arrays across

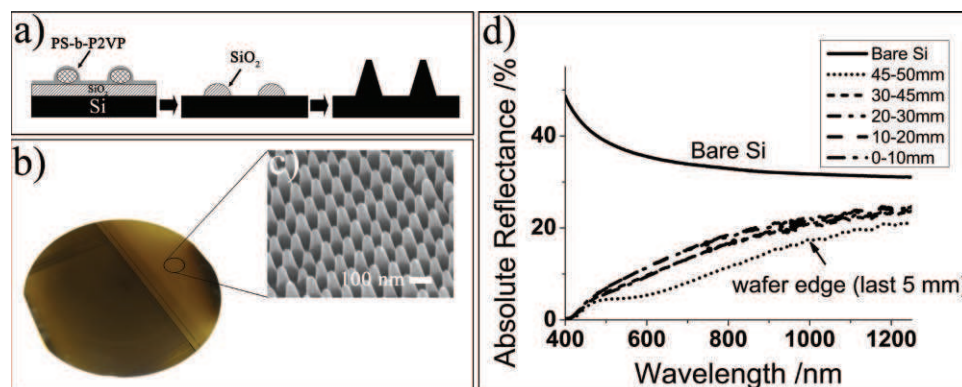


Figure 3. a) Schematic of processing steps for the two step pattern-transfer process used to create silicon pillar arrays over full wafers. b) Picture of 100 mm silicon wafer covered entirely with silicon pillars (the reflected image seen within the wafer is the clean room ceiling). c) SEM image of the silicon pillar arrays. The uniformity of the pillar arrays on the entire wafer can be seen from its uniform color d) Different curves are reflectance spectra of the pillar arrays taken on different spots at varying radial distance from the centre to edge of the wafer.

the wafer is limited only by the uniformity of the original template, and the dry-etching recipe used.

Upon pattern transfer of the full wafer templates shown in Figure 3b, a uniform color was observed across the entire wafer, indicating uniformity in etched Si structures obtained. **Figure 4** shows examples of Si pillar arrays that are not uniform across the wafer. The non-uniformity is inherited from the initial pattern of organic templates, either due to non-optimal spin-coating conditions or presence of dust particles that locally influence self-organization of reverse micelles. Figure 3c shows a representative scanning electron microscopy (SEM) image of the Si pillar arrays on a wafer exhibiting a uniform color throughout. SEM inspection showed pillars with a positively tapered profile, with a feature size of 40 nm at half width, periodicity of 78 nm, and height of 120 nm. The wafer was broken into chips to assess the variation in geometric characteristics of the pillar arrays systematically from centre to edge of the wafer. The SEM inspection confirmed a low variation in nanopillar height, periodicity, and shape across the wafer. However, one of the drawbacks in using SEM in such a case is that it can only measure a few features at one time. This makes it particularly hard to map variations reliably and efficiently across large areas such as full wafers. This limitation affects both SEM as well as AFM imaging. A rapid and economic means of qualifying the uniformity of pillar array characteristics across areas measuring a few tens of micrometers or millimeters

across in a single measurement is therefore desirable. We show that this can be performed reliably using reflectance spectroscopy. Reflectance spectroscopy measures color by recording intensity of reflected light under normal incidence as a function of wavelength. Micro-spectrometers can acquire such spectra on microscopic areas on the surface spanning a few tens of micrometers. Figure 3d shows reflectance measurements carried out at five different points with radially varying distances from the centre to edge of the wafer. An excellent agreement between the curves was obtained with a maximum variation <2% in the reflectance intensities across the entire wavelength range. This is indicative of an excellent uniformity in geometric characteristics of the Si pillar arrays across the full wafer. The maximum variation was observed only at the very edge of the wafer (<5 mm from the edge), possibly due to edge bead formation during spin-coating.

However, a question arises as to how sensitive the reflectance measurements are towards variation of only a few nanometers in Si pillar array characteristics. This was addressed experimentally by measuring the reflectivity of the Si pillar array samples with systematically varying periodicity values. Studying the case of periodicity would suffice in our case given that significant variations in diameter or heights of nanopillars is not expected, based on our earlier discussion and as confirmed by SEM.

Si nanopillar arrays with average periodicities varying in steps of <10 nm could be obtained by varying the periodicity of the reverse micelle arrays. Such a systematic variation in periodicity could be achieved by a variation of concentration of the micelle solution, as discussed before. PS-b-P2VP with mw of 114 kDa, f_{PS} of 0.5 and PDI of 1.08 was used for a proof of concept experiment. The 114 kDa system offered a larger window of variation in pillar periodicity compared to the 80.5 kDa system used before. The Si pillar characteristics were very similar to those obtained with the 80.5 kDa copolymer system, with minor differences in the shape of the pillars. The plot in **Figure 5a** shows the variation of reverse micelle array periodicity as a function of the concentration of the solution used. This is shown for both 114 kDa and 80.5 kDa copolymer systems. Si pillar arrays obtained using the 114 kDa system, and exhibiting three different periodicity values of 91, 83, and 77 nm, are shown in SEM tilt measurements in Figure 5b.

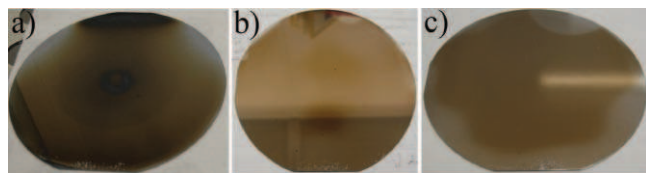


Figure 4. Examples of 100 mm Si wafers with Si nanopillar arrays spanning full wafers, shown in cases of non-uniformity. The non-uniformity can be readily perceived as an optical contrast due to variation in pillar array characteristics across the wafer. The non-uniformity resulted from a) the use of higher acceleration durations (5000 rpm spin speed with an acceleration of 500 rpm/s speeds, 10s acceleration duration) used for coating the copolymer solutions, b) localized defects such as dust particles, or c) edge defects

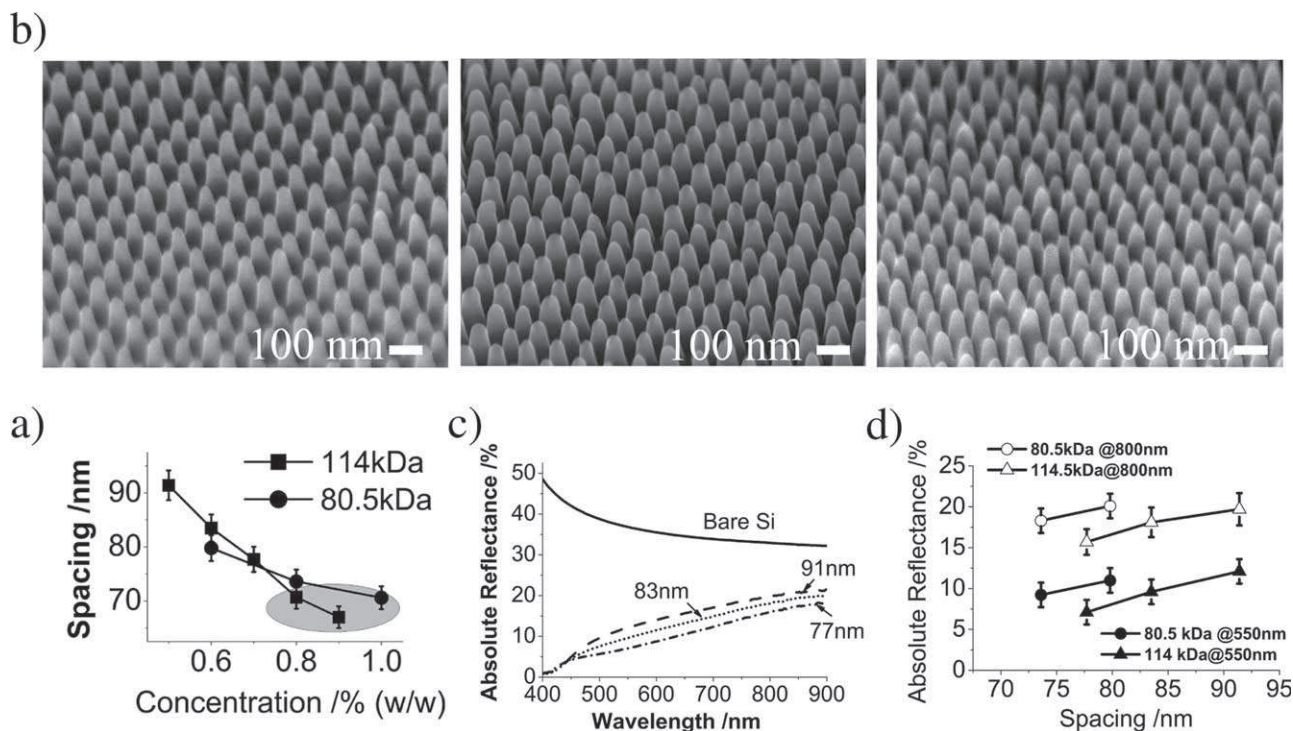


Figure 5. a) Plot showing systematic variation of the periodicity of PS-b-P2VP reverse micelle arrays coated from two different molecular weights, 114 kDa and 80.5 kDa. The masked area denotes pillar arrays with periodicity below 70 nm that were not included for Si pillar fabrication due to inefficient pattern transfer caused by low separation distances. b) SEM tilt measurements showing Si pillar arrays with systematically tunable periodicity obtained from the 114 kDa system. c) Reflectance measurements of Si pillar arrays showing measurably different reflectance curves for periodicity values of 91, 83, and 77 nm. d) Absolute reflectance intensity values of Si pillar arrays plotted as a function of array periodicity, shown for 114 kDa and 80.5 kDa systems at 550 nm and 800 nm wavelengths.

Reflectance measurements performed on these pillars arrays show a clearly distinguishable trend exhibiting a systematic and linear decrease with decreasing periodicity (Figure 5c,d). As shown in the plot in Figure 5d, the average drops in reflectance intensity for every 10 nm decrease in pillar array periodicity were found to be 2.9% and 3.6% at 800 nm and 550 nm, respectively. Assuming this to be also true in the case of pillars obtained with the 80.5 kDa system, then the variation in periodicity across wafer can be estimated to be <5%.

The physical basis for the variation in reflectance with change in Si nanopillar array periodicity lies in the ensuing variation of effective refractive index at the pillar layer that mediates the air–bulk Si interface. This has been investigated by several researchers in the context of controlling reflection by varying the geometry of nanopillar arrays.^[44–46] The dependence of reflectance on geometric parameters of Ge nanopillar arrays grown by vapor–liquid–solid growth is also of interest in this context.^[47,48] Among other variables, volume fraction of nanopillars has been shown to significantly contribute to the effective index. In our case, since the variation of height and diameter across the wafer is low (as confirmed using SEM), the contribution to change in volume fraction could occur mainly by a variation in pillar density. For the 114 kDa system, the density can vary between 130–260 pillars μm^{-2} for periodicity values seen in Figure 5b.

We further employed theoretical modeling and simulations using the rigorous coupled wave analysis (RCWA) method^[49] (Experimental Section) to investigate the response of reflectance spectra to sub-10 nm variations in each of the geometric vari-

ables of the pillar arrays, viz. shape, diameter, height, and periodicity. Figure 6a shows simulated reflectance curves for pillar arrays with various shapes; conical, Gaussian, parabola, or cylinder. The simulations were carried out for nanopillar diameter, height, and periodicity values of 60 nm, 120 nm and 80 nm respectively, which correspond to those of Si pillar arrays shown in Figure 3. The experimental reflectance curve was found to be in excellent agreement with the simulated curve for conical pillar profile. In the next step, reflectance curves for conical pillar profile were simulated for values of height, diameter, and periodicity systematically varied in steps of 5 nm. While investigating the variation with one geometric variable, the other variables were kept constant. The constant values correspond to those of the pillar arrays in Figure 3. The absolute reflectance values at a wavelength of 550 nm, plotted for every 5 nm change in periodicity, height, and diameter of the pillars is shown in Figure 6b. The variation in reflectance values was observed to be linear, with its value decreasing with increase in diameter and height, or with decrease in periodicity. The theoretically observed magnitude of variation in reflectance with periodicity was also found to be in agreement with experiment. The agreement between theory and experiment also supports the fact that the standard deviations in geometric characteristics of the silicon pillar arrays are low enough so that they can be readily modeled to predict their properties. More detailed plots showing the modeled profile, variation of effective refractive index as a function of height, as well as the reflectance curves as a function of differing geometric variables are shown in

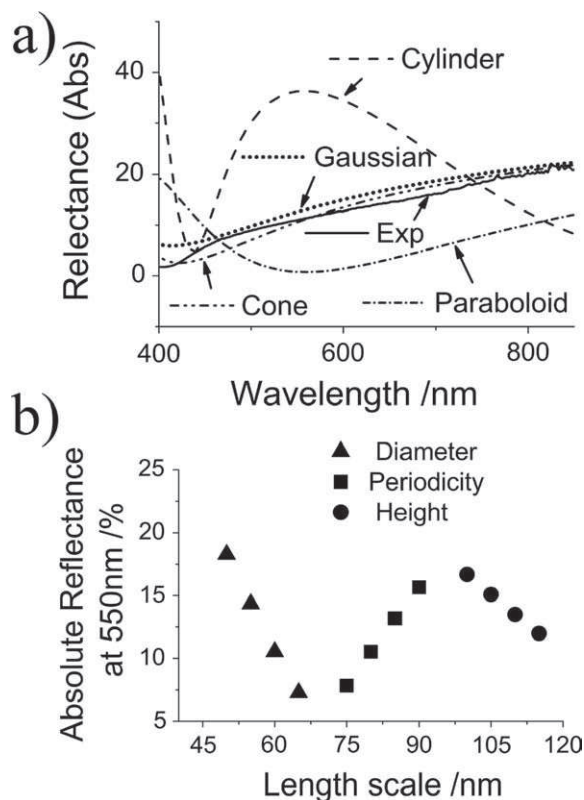


Figure 6. a) Simulated reflectance curves for silicon nanopillar arrays with different shapes presented for diameter, height, and periodicity of 60 nm, 120 nm, and 80 nm. The experimental curve can be seen to agree well with the model of cone, over the entire wavelength. b) Plot of absolute reflectance values at 550 nm simulated for Si nanopillar arrays with a conical profile as a function of systematically varying diameter (height = 120 nm; periodicity = 80 nm), periodicity (diameter = 60 nm; height = 120 nm), and height (diameter = 60 nm; periodicity = 80 nm).

Figure S1 (Supporting Information). Such strong dependency of reflectance spectra on sub-10 nm variations in geometric variables of pillar arrays makes reflectance spectroscopy a unique, high-throughput tool for nanometrology.

Although Si pillar arrays with high uniformity could be achieved over the entire wafer, we found that the pattern transfer was ineffective at low array periodicity values. This is indicated by the shaded portion in Figure 5a. This problem arises when the edge-to-edge separation between the reverse micelles is so low that the hemispherical features are almost touching each other. This makes it difficult to realize well-isolated templates of sufficient mass-thickness contrast necessary for lithographic pattern transfer. In the following section, we describe means of extending this limit in order to achieve robust lithographic templates that perform even with sub-10 nm feature thicknesses or separations. This would allow high spatial resolutions and ultra-low feature separations for the resulting pillar arrays.

4. Robust Lithographic Templates with Feature Thickness and Separation <10 nm

Patterns with high spatial resolutions are in great demand for applications such as data storage, photovoltaic, and plasmonic

devices. For instance, the density of magnetic bits in data storage devices are expected to reach 10 Tb inch⁻², requiring feature width and periodicity of bits to be <10 nm. Nanostructured electrodes in bulk heterojunction photovoltaic devices are required to have a feature width of twice the exciton diffusion length (~20 nm) in order to efficiently separate the electrons and holes before they recombine. Significantly reduced separations are of high interest, even if the feature sizes of the nanostructures are relatively large. For instance, in plasmonic devices (e.g., waveguides, sensors), the electrical field coupling between adjacent metal nanostructures is known to be highly influenced by their separation. Highly sensitive molecular analyte detection by surface-enhanced Raman spectroscopy relies on significant enhancement in electrical field-intensities in 'hot-spots' which are regions in close proximity to multiple metal structures, often with sub-10 nm separations. Therefore, this section is of significant interest, as it demonstrates means of achieving robust lithographic templates with small size and separation. The lithographic pattern transfer shown on Si substrates serves as a proof of concept for the lithographic capability of these templates. The templates are, however, capable of being transferred into several other technologically relevant materials through appropriate post-processing steps, such as ion-beam milling, wet-etching, or in combination with selective growth or deposition processes.

The two-step pattern transfer approach shown to create Si pillar arrays in the earlier section allows for pattern transfer of reverse micelle masks only when the topography or separation of the micelle templates is at least 20 nm. However, such a pattern transfer fails on two accounts: (1) When the micelles are spaced very close to each other, the templates exhibit separation <10 nm from each other resulting in ineffective pattern-transfer. This happens due to insufficient isolation of adjacent features as the separation decreases. The resulting pillar arrays are therefore defective in the sense that they are not well isolated from each other (Figure 7a). This can be seen in the pattern transfer of the templates coated from 1% solution of 80.5 kDa copolymer system, or 0.9% and 1% solution of 114 kDa system (masked area in Figure 5a). (2) When the feature width and the periodicity of the reverse micelle templates are considerably reduced, to approximately 50 nm or below, the template thickness also decreases considerably. With a thickness of ~10 nm or below, the templates lack the capability to withstand the subsequent RIE process and therefore fail (Figure 7b). Both of these challenges can be overcome effectively by substituting the weak organic template with a durable inorganic template.

In the following, we present a means of incorporating a volatile titanium precursor through selective decomposition of the precursor within the core of the reverse micelles. PS-*b*-P4VP (*M_w* 32 kDa, *f_{PS}* 0.78, PDI 1.09) reverse micelles coated from toluene exhibiting both the challenges discussed above, namely edge-to-edge separation and template heights <10 nm, was used for the study. A continuous monolayer as shown in Figure 7b could be obtained by coating at 5000 rpm spin speed, acceleration of 5000 rpm/s, and concentration of 0.3% (w/w). The wafer containing a coating of reverse micelles is exposed to TiCl₄ vapors within an atomic layer deposition (ALD) chamber. The process we describe here however does not involve ALD, but rather a highly controlled chemical vapor deposition (CVD)

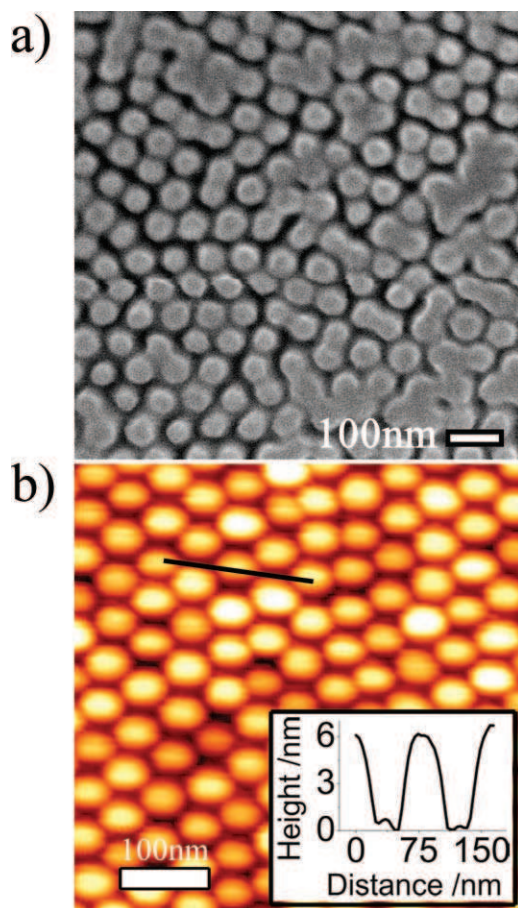


Figure 7. Two major challenges encountered when feature size or separation between the templates is scaled down significantly are illustrated. a) Representative SEM image from top-view showing Si pillar arrays obtained by ineffective pattern transfer caused by close separation between reverse micelle templates. Image shown corresponds to pillar arrays created using templates coated from 1% solution of 80.5 kDa system (Figure 4a, masked area). b) Tapping mode AFM image showing reverse micelle templates with very low values of feature height and separation that are insufficient for lithographic pattern transfer. These arrays correspond to PS-*b*-P4VP (Molecular weight of 32 kDa, $f_{PS} \sim 0.78$) films coated from toluene. Inset shows topography across the marker showing template thickness of only 6 nm.

initiated within the PVP domains of the copolymer. The TiCl_4 concentration was controlled by varying the number of cycles of exposure. Each cycle of exposure consisted of one TiCl_4 pulse and one H_2O pulse each. The exposure durations can be controlled in the range of 10 ms–0.5 s per exposure cycle, with the concentration of TiCl_4 available per square centimeter of the sample controlled down to few nanomoles per cycle. Such a high degree of control over the vapor concentrations allows excellent control over the degree of incorporation of titanium precursor. In three different experiments, the PS-*b*-P4VP coatings were exposed to 10, 20, and 50 cycles of exposure. The TiCl_4 selectively decomposes within the hydrophilic PVP core, thereby strengthening the polymer template towards the RIE of the underlying Si substrate. After incorporation of the titanium precursor, the polymer template could be removed by O_2

plasma RIE to obtain TiO_2 nanoparticle arrays. It can be seen that the particle heights and diameters systematically increase in steps <10 nm with increasing number of vapor-exposure cycles as shown in Figure 8a, b. The thickness of TiO_2 film obtained on flat Si substrate included as a control highlights the controlled growth rates. The TiO_2 nanoparticles exhibit a hemispherical profile (Figure 8a inset), and were clearly isolated in all three cases. The discrete nature of the particles was further confirmed by performing localized EDX analysis on and between the TiO_2 particles in the TEM cross-section (Figure 8c). The EDX curves shown in Figure 8c correspond to the sample with 50 cycles of exposure. The area exposed to EDX appears burnt due to the intense electron beam focused on a small area (Figure 8c inset).

In the next step, we demonstrate nanolithography using the most challenging case, wherein the PS-*b*-P4VP coatings were treated with TiCl_4 vapors for only 10 cycles of exposure. The schematic in Figure 9 shows the steps in the lithographic pattern transfer employed. Two pattern-transfer conditions were employed: PS-*b*-P4VP coatings upon TiCl_4 exposure, (a) without the polymer removal (Figure 9, i–iii), and (b) with polymer removal (using O_2 plasma RIE) to form TiO_2 nanoparticles (Figure 9, iv–v). The TiO_2 nanoparticles obtained in case (b) exhibited height of 7 nm and diameter of 15 nm (Figure 8c, labeled as ‘10cy’). The RIE of Si was effective in both case (a) as well as case (b), proving the effectiveness of the titanium precursor incorporation towards RIE of Si. The pillars obtained using titanium precursor incorporated polymer masks (Figure 9a) were thicker than pillars obtained when pure titania nanoparticle masks (Figure 9b) were used, as expected. Si pillars with feature widths of 32 nm and 25 nm were obtained in cases (a) and (b) respectively (Figure 9a,b). As the periodicity in both cases is the same, the pillars of 32 nm in width exhibited a separation of only 8 nm, while those of 25 nm width exhibited a separation of 15 nm. This provides a subtle means of controlling the feature width and separation between the pillars. Due to the fact that the 32 kDa system also exhibited significantly low separations between the templates, the lithography results presented prove that the cases shown in the masked area in Figure 5a would also work (Figure S2 in Supplementary material).

The TiO_2 nanoparticle masks were found to offer high selectivity towards dry etching of Si using the dry-etch recipes we employed. This allowed high-fidelity pattern transfer with no loss of the feature width of the TiO_2 particles used. This has implications, particularly on the shape of the resulting pillars. The pillars obtained using TiO_2 masks exhibited a distinctly vertical profile, as compared to conical profiles obtained with the polymer templates, for the same Si etching recipe used. The low selectivity in case of polymer template results in translating the hemispherical mask profile into conical profile in the etched structures. The robustness of the mask further determines the maximum duration of etching that can be employed, and therefore the achievable height for the resulting pillars. From the Figure 9, it can be seen that the pillar heights of ~ 100 nm are achieved. At the end of the RIE process, the TiO_2 masks were removed by washing wafers with buffered HF solution. We expect that any remaining TiO_2 is removed mainly by removal of the SiO_2 interface in between the Si pillars and the Titania particle templates. The advantage of the approach shown lies in

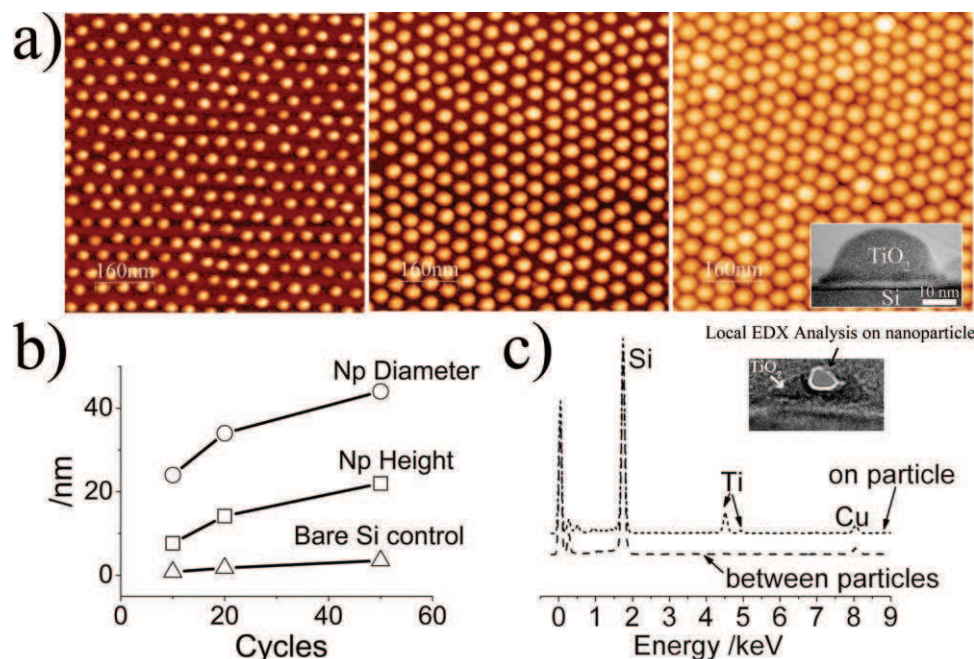


Figure 8. Formation of TiO_2 nanoparticle masks for nanolithography is shown using PS-*b*-P4VP (25000-*b*-7000 g/mol) arrays. a) Tapping mode AFM images of TiO_2 nanoparticle arrays obtained by exposing the PS-*b*-P4VP arrays for 10, 20, and 50 cycles to TiCl_4 vapor followed by removal of the polymeric template using O_2 plasma RIE. TEM cross-section showing the hemispherical profile of TiO_2 nanoparticles is provided as an inset. b) Plot showing highly controlled growth in height and diameter (in steps <10 nm) of TiO_2 nanoparticles as a function of the number of cycles of TiCl_4 exposure used. The thickness of TiO_2 thin film grown on a bare Si substrate under the identical conditions of TiCl_4 vapor exposure is shown as reference. c) Plot shows localized energy dispersive X-ray (EDX) analysis of TiO_2 nanoparticle masks performed in situ using transmission electron microscopy. The clear absence of Ti between particles can be seen. Inset shows the cross section of a TiO_2 nanoparticle with burnt portion corresponding to the spot where EDX analysis was performed.

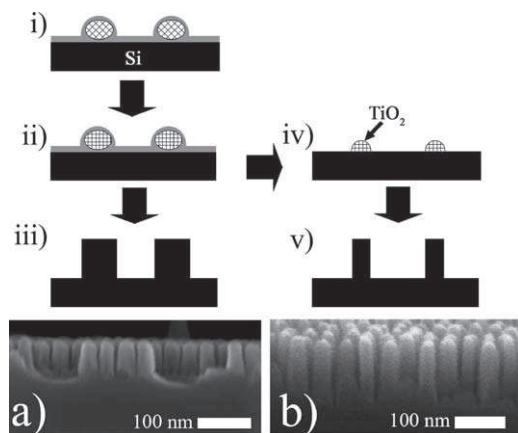


Figure 9. Schematic shows lithographic pattern-transfer process sequence employed to etch Si substrate using PS-*b*-P4VP (25000-*b*-7000 g mol⁻¹) arrays exhibiting features with sub-10 nm thickness and separation. i-iii) schematic of process steps employed for incorporation of TiCl_4 precursor into the polymeric template and used as-such for dry etching. i) as-coated PS-*b*-P4VP micelle arrays ii) After exposure to TiCl_4 vapors iii) Si nanopillar arrays with separation of ~8 nm (SEM cross-section in a)) resulting after pattern-transfer of TiO_2 containing polymer composite into Si by Cl_2 plasma, and subsequent template removal. iv-v) schematic of steps employed to create nascent TiO_2 nanoparticle arrays and their subsequent use as nanolithography templates. iv) TiO_2 nanoparticle arrays obtained upon removal of polymer by O_2 RIE. v) Si nanopillar arrays with a separation of 15 nm (SEM cross-section in b)) obtained upon pattern-transfer of TiO_2 nanoparticle masks into Si and subsequent removal of the mask.

providing a highly controlled, consistent, and precise means of incorporating the precursor, in a manner that does not compromise on the original pattern characteristics.

We note that the formation of TiO_2 nanoparticle has been shown earlier in the literature,^[50] but neither the precursor concentration nor the decomposition can be easily controlled. Based on our observations, even the tiniest variation of the TiO_2 precursor exposure varies the quantity of precursor incorporated. An excess exposure to the precursor can easily compromise the pattern fidelity due to non-selective deposition of TiO_2 . Furthermore, the solution phase approach shown for obtaining TiO_2 particles on surfaces introduces several variables that must be controlled, while also resulting in particles with large standard deviations.^[51,52]

The compatibility of TiO_2 with semiconductor processing techniques makes it an attractive choice for lithographic template, in comparison with metals and transition metal oxides. Therefore the particle arrays of gold or oxides of iron and zinc shown in literature^[53–55] pose a disadvantage in this respect. PS-*b*-PDMS^[56,57] and PS-*b*-PFS^[58,59] can also provide etch contrast due to silicon containing PDMS or PFS blocks. These are however less flexible towards adjustment and fine-tuning due to the inherent limits placed on feature size by the molecular weight and block ratios. This is also true of pure silica nanoparticle arrays produced by selective growth^[60] or deposition^[61] within block copolymer templates. It should further be noted that our approach to such robust lithographic masks can be readily applied to any other diblock copolymer pattern with a hydrophilic block and is therefore very versatile in utility.

Furthermore, the hemispherical geometry of the micelle masks allows for highly controlled variation of the diameter (not only template height) as a function of precursor quantity.

While the inorganic precursor route yields a robust lithographic template, it also involves additional processing due to the vapor phase exposure step. However, this additional step is well justified when lithography employs templates with feature sizes, or separations <10 nm. For templates with larger features or separations, the two-step pattern transfer shown in Figure 3a is still advantageous, as the pattern-transfer can be achieved with a fewer number of steps and by using polymeric templates only.

5. Conclusions

In summary, we have demonstrated highly uniform and robust dot-array templates for nanolithography, exhibiting pattern resolutions down to the sub-50 nm scale, spanning 100 mm Si wafers. The nanopatterns were obtained by exploiting self-assembly and self-organization of polystyrene-block-poly(vinylpyridine), chosen as a model amphiphilic copolymer system. Several issues of high importance to nanopatterning and nanolithography employing the self-assembled templates were addressed in this work. a) Investigation of the relationship between the (mean and width of) distributions of micelle size in solution and the nanopattern variables (topography, diameter, and periodicity) on the surface has led to clearer understanding of the mechanism of pattern formation and the origin of inherent and spatial uniformity of the patterns. b) High-throughput measurements of sub-10 nm variations in geometric characteristics (diameter, periodicity, height, and shape) of lithographically etched Si nanopillar arrays across full wafers were successfully demonstrated. The physical basis of reflectance variation in response to the nanopillar array geometric characteristics was analyzed through theoretical modeling and simulations. This also demonstrated the general capability of reflectance spectroscopy as an effective tool for high-throughput nanometrology. c) Highly controlled and selective vapor phase decomposition of volatile inorganic precursors within block copolymer domains is demonstrated as a promising means of enhancing integrity and robustness of the templates for nanolithography at high pattern resolutions. This was shown using TiCl_4 decomposition within PVP domains to form TiO_2 nanoparticle templates exhibiting tunability of size (height and diameter) in steps <10 nm. The lithographic capability using this approach was demonstrated for template heights as small as 6 nm and separations of ~8 nm. The techniques and concepts required to derive nanolithography templates demonstrated throughout this report are general in nature, and have a high potential for exploitation in a wide array of applications where uniform, high-density nanopatterns are sought, e.g., batteries, solar-cells, light-emitting diodes, self-cleaning surfaces, non-volatile memory devices, and plasmonic biosensors.

6. Experimental Section

Materials: All polymers were purchased from Polymer Source Inc. (Montreal, Canada) and used without further purification. Toluene and

m-xylene were obtained as anhydrous solvents with purity >99% from Sigma-Aldrich Pte Ltd. Prime grade silicon wafers were obtained from Silicon Valley Microelectronics (Santa Clara, CA, USA). Point Probe Plus silicon tips for tapping mode imaging measurements with atomic force microscopy were purchased from Nanosensors (Neuchatel, Switzerland).

Methods: The silicon substrates were cleaned by ultrasonication in acetone followed by 2-propanol and finally treated with UV/ozone for 10 min. Spin-coating was carried out in CEE model 100CB spinner (Brewer Science Inc., MO, USA). Polymer solutions were prepared by dissolving the polymer in respective solvents, and were stirred until dissolution. The solutions were coated at a relative humidity of 55% and ambient temperature of 22 °C. Vapour phase exposure to create TiO_2 masks was carried out in home-built atomic layer deposition equipment. N_2 gas was used both as a carrier gas and purge gas. TiCl_4 and H_2O (de-ionized water) were introduced into a viscous flow ALD chamber in pulses. The length of each pulse (or exposure duration) precisely determines the amount of precursor available for the surface adsorption. The vapor concentration per pulse can be controlled down to nano moles per pulse by controlling the exposure duration. This duration in turn can be estimated from the vapor pressure of precursor (using the Antoine equation, $\log(p) = A - (B / (T + C))$, where P is vapor pressure in bar, T is temperature in Kelvin and coefficients A , B and C are obtained from the NIST Chemistry Web book) and the flux of gas molecules impinging on the surface (using equation: $J (\text{m}^2 \text{s}^{-1}) = P \sqrt{(2\pi mkT)}$, where m = molecular mass, k = Boltzmann constant). For TiCl_4 , these values were estimated to be $P = 12.4$ Torr and $N = 1.839 \times 10^{21}$ molecules/ $\text{cm}^2 \text{s}$). For the two step pattern transfer process, the polymer templates were first transferred into underlying SiO_2 film of 25 nm thickness by dry etching using $\text{C}_4\text{F}_8/\text{CH}_4$ for 10 s duration using AMS 200 DSE, an inductively coupled plasma (ICP) etcher (Alcatel Micromachining Systems, Annecy, France). The subsequent Si etching was carried out using Cl_2 plasma for 30 s duration using STS etcher (Surface Technology Systems, New Port, UK). The etching recipe for Si was common for both the two-step transfer, and for pattern-transfer of TiO_2 nanoparticle patterns into silicon substrate. The polymer patterns were characterized using DI 3100 atomic force microscopy (Veeco Instruments Inc., NY, USA) equipment operated in tapping mode. Image analysis and production was performed using in-built DI 5.12 version software from Veeco, ImageJ (National Institutes of Health, USA) and WSxM 4.0^[62] (Nanotec Electronica S.L., Spain). X-ray photoelectron spectroscopy (XPS, VG ESCALab 220i-XL) was carried out to confirm the absence of TiO_2 when the Si nanopillar arrays were obtained following steps shown in Figure 9. SEM was performed using JSM-6700F FESEM (JEOL, Tokyo, Japan). Transmission electron microscopy was performed using Philips CM300 TEM operating at 300 kV and equipped with DX4 EDS system and Gatan Filter. Light scattering measurements were performed using BI-200SM Research Goniometer System (Brookhaven Instruments Corporation, NY, USA) equipped with 633 nm laser. Reflectance measurements were carried out using a micro-spectrometer from CRAIC (Craic Technologies, CA, USA). The samples were measured on areas of $77 \mu\text{m} \times 77 \mu\text{m}$. Bulk Si samples were used as a reference, to obtain absolute reflectance data. The optical modelling of reflectance spectra were performed using multilayer model as used before in literature.^[44,63] The pillar arrays were divided into 100 imaginary layers, and the effective refractive index of each layer was calculated using effective medium approximation.^[64] The reflectance of the whole system was then calculated by solving Maxwell's equations of the multilayer system. More details can be found in the Supporting Information.

Supporting Information

Supporting Information is available from the Wiley Online Library or from the author.

Acknowledgements

The authors gratefully acknowledge Dr. Gao Han (IMRE) for helpful discussions, and help with chamber used for vapor phase exposure experiments.

Received: November 11, 2010

Revised: December 1, 2010

Published online: February 25, 2011

- [1] Z. Fan, H. Razavi, J. W. Do, A. Moriwaki, O. Ergen, Y. L. Chueh, P. W. Leu, J. C. Ho, T. Takahashi, L. A. Reichertz, S. Neale, K. Yu, M. Wu, J. W. Ager, A. Javey, *Nat. Mater.* **2009**, *8*, 648.
- [2] S. A. Maier, H. A. Atwater, *J. Appl. Phys.* **2005**, *98*.
- [3] A. Alizadeh, D. Hays, S. T. Taylor, C. Keimel, K. R. Conway, L. Denault, K. Krishnan, V. H. Watkins, R. Neander, J. S. Brown, A. Stintz, S. Krishna, M. Blumin, I. Saveliev, H. E. Ruda, E. Braunstein, C. Jones, *J. Appl. Phys.* **2009**, *105*.
- [4] H. H. Wang, C. Y. Liu, S. B. Wu, N. W. Liu, C. Y. Peng, T. H. Chan, C. F. Hsu, J. K. Wang, Y. L. Wang, *Adv. Mater.* **2006**, *18*, 491.
- [5] C. K. Chan, H. Peng, G. Liu, K. McIlwrath, X. F. Zhang, R. A. Huggins, Y. Cui, *Nat. Nanotechnol.* **2007**, *3*, 31.
- [6] H. D. Tong, H. V. Jansen, V. J. Gadgil, C. G. Bostan, E. Berenschot, C. J. M. Van Rijn, M. Elwenspoek, *Nano Lett.* **2004**, *4*, 283.
- [7] C. A. Ross, *Annu. Rev. Mater. Sci.* **2001**, *31*, 203.
- [8] R. F. Pease, S. Y. Chou, *Proc. IEEE* **2008**, *96*, 248.
- [9] G. M. Wallraff, W. D. Hinsberg, *Chem. Rev.* **1999**, *99*, 1801.
- [10] J. I. Martin, J. Nogues, K. Liu, J. L. Vicent, I. K. Schuller, *J. Magn. Mater.* **2003**, *256*, 449.
- [11] X.-M. Yan, A. M. Contreras, M. M. Koebel, J. A. Liddle, G. A. Somorjai, *Nano Lett.* **2005**, *5*, 1129.
- [12] G. M. Kim, M. A. F. Van Den Boogaart, J. Brugger, *Microelectron. Eng.* **2003**, *67–8*, 609.
- [13] F. S. Bates, G. H. Fredrickson, *Phys. Today* **1999**, *52*, 32.
- [14] R. A. Segalman, *Mater. Sci. Eng. R.* **2005**, *R48*, 191.
- [15] I. W. Hamley, *Nanotechnology* **2003**, *14*, R39.
- [16] M. Park, C. Harrison, P. M. Chaikin, R. A. Register, D. H. Adamson, *Science* **1997**, *276*, 1401.
- [17] C. J. Hawker, T. P. Russell, *MRS Bull.* **2005**, *30*, 952.
- [18] U. Jeong, H. C. Kim, R. L. Rodriguez, I. Y. Tsai, C. M. Stafford, J. K. Kim, C. J. Hawker, T. P. Russell, *Adv. Mater.* **2002**, *14*, 274.
- [19] S. H. Tung, T. Xu, *Macromolecules* **2009**, *42*, 5761.
- [20] W. K. Li, S. Yang, *J. Vac. Sci. Technol. B.* **2007**, *25*, 1982.
- [21] S. Krishnamoorthy, R. Pugin, J. Brugger, H. Heinzelmann, C. Hinderling, *Adv. Funct. Mater.* **2006**, *16*, 1469.
- [22] P. Mansky, P. Chaikin, E. L. Thomas, *J. Mater. Sci.* **1995**, *30*, 1987.
- [23] S. Krishnamoorthy, R. Pugin, J. Brugger, H. Heinzelmann, A. C. Hoogerwerf, C. Hinderling, *Langmuir* **2006**, *22*, 3450.
- [24] S. Krishnamoorthy, Y. Gerbig, C. Hibert, R. Pugin, C. Hinderling, J. Brugger, H. Heinzelmann, *Nanotechnology* **2008**, *19*, 85301.
- [25] J. P. Spatz, T. Herzog, S. Mossmer, P. Ziemann, M. Moller, *Advanced Materials* **1999**, *11*, 149.
- [26] G. Riess, *Progr. Polym. Sci.* **2003**, *28*, 1107.
- [27] S. Krishnamoorthy, R. Pugin, J. Brugger, H. Heinzelmann, C. Hinderling, *Adv. Funct. Mater.* **2006**, *16*, 1469.
- [28] C. L. Haynes, R. P. Van Duyne, *J. Phys. Chem. B* **2003**, *107*, 7426.
- [29] K. W. Guarini, C. T. Black, S. H. I. Yeung, *Adv. Mater.* **2002**, *14*, 1290.
- [30] K. W. Guarini, C. T. Black, S. H. I. Yeung, *Adv. Mater.* **2002**, *14*, 1290.
- [31] T. H. Kim, J. Hwang, W. S. Hwang, J. Huh, H. C. Kim, S. H. Kim, J. M. Hong, E. L. Thomas, C. Park, *Adv. Mater.* **2008**, *20*, 522.
- [32] C. J. Lawrence, W. Zhou, *J. Non-Newtonian Fluid Mech.* **1991**, *39*, 137.
- [33] H. Watanabe, M. L. Yao, T. Sato, K. Osaki, *Macromolecules* **1997**, *30*, 5905.
- [34] W. W. Flack, D. S. Soong, A. T. Bell, D. W. Hess, *J. Appl. Phys.* **1984**, *56*, 1199.
- [35] J. A. Britten, I. M. Thomas, *J. Appl. Phys.* **2009**, *71*, 972.
- [36] B. R. Murthy, J. K. K. Ng, E. S. Selamat, N. Balasubramanian, W. T. Liu, *Biosens. Bioelectron.* **2008**, *24*, 723.
- [37] S. Chang, J. Oh, S. T. Boles, C. V. Thompson, *Appl. Phys. Lett.* **2010**, *96*, 153108.
- [38] C. T. Black, K. W. Guarini, K. R. Milkove, S. M. Baker, T. P. Russell, M. T. Tuominen, *Appl. Phys. Lett.* **2001**, *79*, 409.
- [39] A. S. Aric3, P. Bruce, B. Scrosati, J. M. Tarascon, W. Van Schalkwijk, *Nat. Mater.* **2005**, *4*, 366.
- [40] J. S. Huang, C. Y. Hsiao, S. J. Syu, J. J. Chao, C. F. Lin, *Sol. Energy Mater. Sol. Cells* **2009**, *93*, 621.
- [41] V. Gowrishankar, S. R. Scully, A. T. Chan, M. D. McGehee, Q. Wang, H. M. Branz, *J. Appl. Phys.* **2008**, *103*, 064511.
- [42] V. Poborchii, T. Tada, T. Kanayama, A. Moroz, *Appl. Phys. Lett.* **2003**, *82*, 508.
- [43] C. T. Black, K. W. Guarini, Y. Zhang, H. J. Kim, J. Benedict, E. Sikorski, I. V. Babich, K. R. Milkove, *IEEE Electron. Device Lett.* **2004**, *25*, 622.
- [44] D. G. Stavenga, S. Foletti, G. Palasantzas, K. Arikawa, *Proc. R. Soc. B.* **2006**, *273*, 661.
- [45] C. H. Sun, P. Jiang, B. Jiang, *Appl. Phys. Lett.* **2008**, *92*, 061112.
- [46] W. L. Min, B. Jiang, P. Jiang, *Adv. Mater.* **2008**, *20*, 3914.
- [47] Y. L. Chueh, Z. Fan, K. Takei, H. Ko, R. Kapadia, A. A. Rathore, N. Miller, K. Yu, M. Wu, E. E. Haller, *Nano Lett.* **2009**, *10*, 520.
- [48] Z. Fan, R. Kapadia, P. W. Leu, X. Zhang, Y. L. Chueh, K. Takei, K. Yu, A. Jamshidi, A. A. Rathore, D. J. Ruebusch, *Nano Lett.* **2010**, *10*, 3823.
- [49] M. G. Moharam, E. B. Grann, D. A. Pommet, T. K. Gaylord, *J. Opt. Soc. Am. A* **1995**, *12*, 1068.
- [50] X. Li, K. H. A. Lau, D. H. Kim, W. Knoll, *Langmuir* **2005**, *21*, 5212.
- [51] Z. C. Sun, D. H. Kim, M. Wolkenhauer, G. G. Bumbu, W. Knoll, J. S. Gutmann, *ChemPhysChem* **2006**, *7*, 370.
- [52] L. Song, Y. M. Lam, C. Boothroyd, P. W. Teo, *Nanotechnology* **2007**, *18*, 135605.
- [53] J. P. Spatz, S. Mossmer, C. Hartmann, M. Moller, T. Herzog, M. Krieger, H. G. Boyen, P. Ziemann, B. Kabius, *Langmuir* **2000**, *16*, 407.
- [54] R. Glass, M. Moller, J. P. Spatz, *Nanotechnology* **2003**, *14*, 1153.
- [55] S. I. Yoo, B. H. Sohn, W. C. Zin, S. J. An, G. C. Yi, *Chem. Comm.* **2004**, 2850.
- [56] Y. S. Jung, C. A. Ross, *Nano Lett.* **2007**, *7*, 2046.
- [57] C. C. Chao, T. C. Wang, R. M. Ho, P. Georgopoulos, A. Avgeropoulos, E. L. Thomas, *ACS Nano* **2010**, *4*, 2088.
- [58] M. A. Hempenius, R. G. H. Lammertink, M. Peter, G. J. Vancso, *Macromol. Symp.* **2003**, *196*, 45.
- [59] J. Y. Cheng, C. A. Ross, E. L. Thomas, H. I. Smith, G. J. Vancso, *Appl. Phys. Lett.* **2002**, *81*, 3657.
- [60] H. C. Kim, X. Jia, C. M. Stafford, D. H. Kim, T. J. McCarthy, M. Tuominen, C. J. Hawker, T. P. Russell, *Adv. Mater.* **2001**, *13*, 795.
- [61] H. Yoo, S. Park, *Nanotechnology* **2010**, *21*, 245304.
- [62] I. Horcas, R. Fernandez, J. M. Gomez-Rodriguez, J. Colchero, J. Gomez-Herrero, A. M. Baro, *Rev. Sci. Instrum.* **2007**, *78*, 013705.
- [63] W. L. Min, P. Jiang, B. Jiang, *Nanotechnology* **2008**, *19*, 475604.
- [64] D. A. G. Bruggeman, *Ann. Phys.* **1935**, *24*, 132.